CO₂-crystal wettability in potassic magmas: implications for eruptive dynamics in light of experimental evidence for heterogeneous nucleation

Gianluca Sottili,[1] Sara Fanara,[2] Aurora Silleni,[3,4] Danilo M. Palladino[3] and Burkhard C. Schmidt[2]

[1]*Istituto di Geologia Ambientale e Geoingegneria IGAG-CNR, Via Salaria km* 29,300, *Rome, Italy. E-mail: gianluca.sottili@uniroma1.it*
[2]*Institut für Mineralogie, GZG, Universität Göttingen, Goldschmidtstr.* 1, *Göttingen, Germany*
[3]*Dipartimento di Scienze della Terra, Sapienza-Università di Roma, Piazzale Aldo Moro* 5, *Rome, Italy*
[4]*Dipartimento di Scienze–Sezione Geologia, Università Roma Tre, Largo San Leonardo Murialdo* 1, *Roma, Italy*

SUMMARY

The volatile content in magmas is fundamental for the triggering and style of volcanic eruptions. Carbon dioxide, the second most abundant volatile component in magmas after H_2O, is the first to reach saturation upon ascent and depressurization. We investigate experimentally CO_2-bubble nucleation in trachybasalt and trachyte melts at high temperature and high pressure (*HT* and *HP*) through wetting-angle measurements on different (sialic, mafic or oxide) phenocryst phases. The presence of crystals lowers the supersaturation required for CO_2-bubble nucleation up to 37 per cent (heterogeneous nucleation, *HeN*), with a minor role of mineral chemistry. Different from H_2O-rich systems, feldspar crystals are effective in reducing required supersaturation for bubble nucleation. Our data suggest that leucite, the dominant *liquidus* phase in ultrapotassic systems at shallow depth (i.e. <100 MPa), facilitates late-stage, extensive magma vesiculation through CO_2 *HeN*, which may explain the shifting of CO_2-rich eruptive systems towards an apparently anomalous explosive behaviour.

Key words: Magma chamber processes; Explosive volcanism; Volcanic gases.

INTRODUCTION

The kinetics of volatile separation from magma through bubble nucleation and growth controls the intensity and style of volcanic eruptions (Scandone 1996; Bower & Woods 1997). Constraining the controlling factors for magma vesiculation is fundamental to reconstruct the trigger mechanisms of explosive volcanism during ascent from the magma chamber to the fragmentation level. Carbon dioxide, the second most abundant volatile species in magmas, can affect significantly magma saturation conditions (Holloway 1976; Wilson *et al.* 1980; Papale 1999; Papale & Polacci 1999). Experimental data indicate that, due to the much lower CO_2 solubility compared to H_2O, the volatile saturation in presence of CO_2 is reached at higher pressure; also, the difference between the volatile saturation pressure and the critical pressure for initiating the bubble nucleation (i.e. the critical supersaturation), increases with decreasing H_2O content or increasing CO_2 content in rhyolitic melts (Mourtada-Bonnefoi & Laporte 2002). As a consequence, the relatively lower CO_2 solubility controls, for increasing CO_2 contents and in presence of water, a relatively earlier (i.e. deeper) nucleation event in the magma with respect to CO_2-free systems. The deeper onset of vesiculation can lead to extensive gas loss through wall

rocks and/or magma column (Jaupart 1998; Navon & Lyakhovsky 1998), thus preventing large degrees of volatile supersaturation and reducing the explosive potential (Mourtada-Bonnefoi & Laporte 2002). Another important effect on the dynamics of magma ascent in explosive eruptions is that an increase of the $[CO_2]/[H_2O]$ ratio produces an increase in the exit gas volume fraction and depth of the fragmentation level (Papale & Polacci 1999). Also, enhanced CO_2 degassing observed prior to powerful explosive events in mafic volcanoes (e.g. at Stromboli) has been attributed to the exsolution from a deeply stored magmas, leading to the transition from effusive to explosive activity (Aiuppa *et al.* 2010).

Increasing evidence points out diffuse limestone assimilation and CO_2 release for a variety of volcanic systems (Freda *et al.* 1997; Goff *et al.* 2001; Deegan *et al.* 2010; Jeffery *et al.* 2013; Jolis *et al.* 2015) and carbonate break-down and assimilation processes are gaining interest as driving mechanisms for enhancing the intensity of explosive volcanic eruptions (Freda *et al.* 2011; Jolis *et al.* 2015). In particular, the unusually explosive behaviour of low-viscosity, mafic magmas (SiO_2 even <42 wt.%) at the ultrapotassic Colli Albani volcanic district (central Italy) has been related to significant CO_2 addition from carbonate wall rocks (Freda *et al.* 1997, 2011). This process has been also proposed to explain the intensity of the

79 AD Pompeii and 472 AD Pollena eruptions at Somma-Vesuvius (Jolis *et al.* 2015) and at other volcanoes (e.g. Popocatépetl, Merapi and Kelut; Goff *et al.* 2001; Deegan *et al.* 2010; Jeffery *et al.* 2013). Thus, in volcanic systems emplaced in carbonate-rich crust, the CO_2 assimilation from magma–carbonate interaction due to contact reactions at relatively shallow depths may significantly affect the eruptive dynamics (Freda *et al.* 1997, 2011; Goff *et al.* 2001; Deegan *et al.* 2010; Jeffery *et al.* 2013; Jolis *et al.* 2015). In this case, CO_2 intake from wall rocks may largely prevail over gas escape due to relative bubble floatation and rock permeability (Sottili *et al.* 2010; Freda *et al.* 2011). Thus, a relatively early (i.e. deeper) bubble nucleation event in the magma may result in a substantial density decrease and buoyancy increase of the magma at relatively greater depths. In this perspective, understanding the kinetics of CO_2 degassing, from bubble nucleation to magma fragmentation, is fundamental for reconstructing hazardous scenarios related to explosive volcanism.

In presence of crystals, H_2O bubbles may nucleate more easily in the magma because of a reduction of surface tension, σ, at the bubble-crystal interface (Hurwitz & Navon 1994; Lasaga 1998; Navon & Lyakhovsky 1998). For example, in hydrated rhyolitic melts, the presence of microcrystals of Fe-Ti oxides, acting as efficient *HeN* sites (Gualda & Anderson 2007), reduces the decompression required for homogenous nucleation from >10 to <1 MPa (Hurwitz & Navon 1994). In CO_2-dominated silicate melts, the role of mineral phase chemistry on the efficiency of *HeN* may differ significantly with respect to H_2O-saturated melts. However, up to now, little is known about the extent of *HeN* of CO_2 on crystal surfaces in silicate melts.

Here we report the results of *HP-HT* decompression experiments on CO_2-saturated trachybasalt and trachytic melts, as representative of the compositional end-members of potassic suites, to evaluate the role of crystalline phases and melt composition on CO_2 bubble nucleation through wetting angle measurements on different crystal types (e.g. sialic, mafic or oxide). Experimental procedure of decompression experiments are described in detail in Fanara *et al.* (2016). When compared to H_2O-dominated silicate melts, the experimental evidence shows that mineral chemistry plays a minor role in CO_2-saturated melts for the efficiency of crystals as sites for bubble nucleation. In addition, in contrast to H_2O-saturated silicate melts, where sialic crystals affect very little H_2O bubble nucleation, leucite, plagioclase and K-feldspar crystals are efficient sites for *HeN*, thus facilitating the formation of CO_2 bubbles.

THEORETICAL BACKGROUND

The formulation of the classical nucleation theory benefited of the fundamental contribution of Gibbs, Laplace, Kelvin and many others. A detailed treatment of this theory can be found in Dunning (1969), Hirth *et al.* (1970) and Landau & Lifshitz (1980). Specifically, the nucleation process can be described by the classical nucleation theory assuming that the thermodynamic properties (e.g. energy, pressure, temperature, chemical potential and surface tension) of the new phase (bubble nuclei) at the nanometric scale match those of macroscopic systems. For example, the surface energy associated with a newly formed bubble nucleus surface, A, is simply $A\sigma$, where σ is the surface tension measured in a macroscopic system (e.g. Navon & Lyakhovsky 1998).

When the surface energy of the crystal–gas interface is lower than that of the melt–gas interface, the energy required for heterogeneous nucleation on crystal surfaces is lower than that required for homogeneous nucleation (HoN). Thus, the critical degree of supersaturation, ΔP, in crystal-bearing magmas can be much lower than ΔP in crystal-free magmas. The activation energy required for heterogeneous bubble nucleation, ΔF, is:

$$\Delta F = \frac{16\pi\sigma^3}{3\Delta P^2}\phi, \tag{1}$$

where σ is the surface tension of the gas-melt interface, ΔP is the difference between the volatile saturation pressure and the critical pressure for bubble nucleation and ϕ is a factor associated with the nucleation of bubbles on crystal surfaces (*HeN*) amounting to:

$$\phi = \frac{(2-\cos\vartheta)(1+\cos\vartheta)^2}{4}, \tag{2}$$

where ϑ is the wetting angle defined as the angle between the crystal face and the tangent to the bubble face at the contact, measured through the melt (e.g. Navon & Lyakhovsky 1998). The presence of crystals in the melt may lower considerably the supersaturation required for bubbles nucleation. For example, when the vapour wets the crystal completely, $\vartheta = 180°$ and no supersaturation is required for bubbles to nucleate. When the shape of the bubble nucleus is a half-sphere, $\phi = 0.5$ and the presence of crystals reduces the ΔF required for homogeneous nucleation to half. When crystals are not wetted by bubbles, then $\phi = 1$ and the presence of the crystals does not influence nucleation. In addition to the wetting angle, crystal morphology also plays a key role in determining the efficiency of nucleation due to variable surface roughness (Zhou & De Hosson 1995).

Eq. (1) applies to both nanoscopic and microscopic bubbles wetting the surfaces of a given solid phase, thus measurements of contact angles at microscale provide a proxy to investigate nanoscale phenomena, for example the process of bubble nucleation on crystal surfaces (Navon & Lyakhovsky 1998). Some research groups reported anomalous contact angles of nanobubbles with respect to micrometric bubbles (e.g. Yang *et al.* 2007; Li *et al.* 2014). However surface tension, σ, at the gas–melt interface does not change with bubble size (Ducker 2009), thus wetting angle measurements for bubbles with radius much grater than the critical radius represent a suitable proxy to estimate quantitatively the relative efficiency of mineral phases as sites for *HeN*.

EXPERIMENTAL AND ANALYTICAL TECHNIQUES

Trachyte and trachybasalt glasses from the Campi Flegrei Volcanic District, previously characterized for H_2O-CO_2 solubility by Fanara *et al.* (2015), were used as starting materials (see Table 1 for details). Volatile-free glasses were doped with $Ag_2C_2O_4$ in order to obtain a CO_2-saturated melt and were synthesized in an Internally Heated Pressure Vessel (IHPV), equipped with a decompression system and a rapid-quench device, at $T = 1200\ °C$ and 300 MPa for 48 hr at relatively oxidizing conditions (typically between NNO+2 and NNO+4; for example Schmidt *et al.* 1997; Schuessler *et al.* 2008).

The obtained CO_2-bearing glasses were powdered and sealed into $Au_{75}Pd_{25}$ capsules together with millimetre-sized crystals typical of potassic systems, that is: olivine, clinopyroxene, K-feldspar, leucite and Cr-spinel. In addition to the crystals added initially, in the experimental products we found new-formed microcrystallline phases of olivine, plagioclase and Fe-Ti oxides (Table 2).

Table 1. Composition of trachytic and trachybasaltic melts measured by electron microprobe (from Fanara *et al.* 2015).

Sample	Trachyte	Trachybasalt
SiO_2	60.31 (48)	49.03 (45)
TiO_2	0.42 (1)	1.28 (12)
Al_2O_3	18.32 (46)	16.10 (55)
FeO^a	5.21 (16)	8.71 (61)
CaO	4.11 (10)	12.13 (48)
MgO	1.31 (13)	8.50 (34)
Na_2O	2.81 (16)	2.85 (19)
K_2O	7.47 (17)	1.56 (6)
Total	100.08	100.16
NBO/T	0.17	0.71

Notes: Microprobe analyses are based on 30 measurements on three fragments of each glass. One standard deviation is given in parentheses and refers to the last two decimal places.
^{a}All iron is given as FeO.

To simulate the ascent of magma in a volcanic conduit, the samples were initially equilibrated at $P = 300$ MPa and at T between 1128 and 1156 °C for durations between 15 and 45 hr, followed by a continuous decompression with a rate of about 4 MPa min^{-1} to a final pressure of 30 MPa. Pressure was measured by a pressure transducer and was typically oscillating ±0.1 MPa; temperature was measured using S-type thermocouples and was typically oscillating ±3 °C. As soon as the final pressure was reached, the samples were drop-quenched isobarically leading to a cooling rate of about 50–150 °C s^{-1}. Some experiments were rapidly quenched directly from the initial conditions without decompression to check the vesicularity features of the samples at the initial equilibrium conditions.

After the experiments, the samples were cut into pieces, embedded into epoxy and polished. The two-dimensional textural parameters, such as bubble size and shape, vesicularity and wetting angles were obtained from electron-optical images collected by a FEI Quanta 400 and a by Leo1455VP scanning electron microscopes (SEM) and analysed using the ImageJ software (developed by *W. Rasband*, NIH, http://rsb.info.nih.gov/ij). Crystal phase compositions were analysed by Energy Dispersive X-ray analyses (EDX). Volatile contents in bubble and crystal-poor glasses were analysed by Fourier Transform Infrared Spectroscopy (FTIR) using a FTIR spectrometer Bruker IFS88 equipped with an IR-ScopeII at the Institute of Mineralogy at the University of Hannover. The bulk carbon content in the CO_2-bearing starting glasses was analysed using a Carbon-Sulfur Analyzer (CSA) at the Institute of Mineralogy at the University of Hannover. To infer the composition of volatiles present in the vesicles of the starting materials and of the decompressed samples, Raman spectra were collected using a Horiba Labram HR UV Raman Spectrometer equipped with a 488 nm solid-state laser.

Focusing the laser beam of the Raman on several closed bubbles just below the surfaces of the decompressed samples, we determined a volatile composition in the vesicles of about 90 per cent CO_2 (plus 10 per cent N_2 from air initially trapped in the capsule, in the powder pore spaces). Specifically, here we analyze the wettability of crystals by CO_2 through wetting angle measurements, as we assume the surface tension, σ, controlling CO_2 wetting angles as scale-independent (i.e. constant for both nanometric nuclei and micrometric CO_2 bubbles). A complication to the determination of wetting angles arises since the measured values are apparent angles resulting from the intersection of 3-D crystal-bubble textures with

Table 2. Summary of experimental conditions and wetting angles measurements for individual mineral phases (including added crystals of olivine, clinopyroxene, Cr-spinel, leucite and K-feldspar, and new-formed microcrystals of olivine, plagioclase and Fe-Ti oxides). All the decompression experiments were equilibrated at approx. $P = 300$ MPa and T between 1125 and 1150 °C for run durations of 15–45 hr, followed by a decompression with a rate of 4 MPa min^{-1} to a final pressure of ~30 MPa.

Melt composition	Crystal	Sample	n.*	ϑ (mean ± SDM)	Median (50th percentile)	$\Delta P_{HeN}/\Delta P_{HoN}$**	$\Delta P_{HeN}/\Delta P_{Hom}$***
Trachyte	*Clinopyroxene*	DTA1.3 DTA8 DTA12 DTA11.3	249	49° ± 1°	47°	0.92 ± 0.01	0.80 ± 0.01
	Cr-spinel	DTA1.3 DTA3.2	131	63 ± 1°	62°	0.81 ± 0.01	0.70 ± 0.01
	Leucite	DTA11.3 DTA11.1	109	55° ± 1°	55°	0.88 ± 0.01	0.76 ± 0.01
	K-feldspar	DTA11.2	66	70° ± 2°	73°	0.72 ± 0.03	0.63 ± 0.03
Trachybasalt	*Clinopyroxene*	DTS2.2 DTS5 DTS4.3	98	57° ± 1°	56°	0.86 ± 0.01	0.75 ± 0.01
	Olivine	DTS2.1 DTS5	28	47° ± 3°	50°	0.92 ± 0.02	0.80 ± 0.02
	Plagioclase	DTS2.2 DTS5	5	48° ± 3°	50°	0.91 ± 0.03	0.79 ± 0.03
	Cr-spinel	DTS2.1 DTS5	47	60° ± 3°	60°	0.82 ± 0.03	0.71 ± 0.03
	Fe-Ti oxides	DTS4.4	27	51° ± 2°	50°	0.90 ± 0.01	0.78 ± 0.01

Notes: n.* is the number of ϑ measurements; $\Delta P_{HeN}/\Delta P_{Hom}$ values refer to bubble nucleation on smooth crystal surfaces (**) and crystal edges (mean values) (***); for fixed ΔP and σ values, $\Delta P_{HeN}/\Delta P_{HoN}$ is proportional to $\phi^{0.5}$ (see eq. 2 in the text). SDM is the standard deviation of the mean. The effects of crystal edges on $\Delta P_{HeN}/\Delta P_{Hom}$ values, as reported in Fig. 1, are calculated following Sigbee (1969).

Table 3. Capsule assemblage and volatile concentrations in the starting materials.

Sample (Trachyte)	Glass powder (mg)	$Ag_2C_2O_4$ (mg)	CO_2 (mg)	CO_2 (%)	CO_2 (CSA, %)	CO_2 (MIR, %)	CO_3^{2-} (MIR, %)	H_2O (MIR, %)
DTA6	791	12.8	3.17	0.40	0.20(3)	–	0.132(15)	0.70(25)
DTA10	802	8.22	2.04	0.25	0.26(4)	0.05(2)	0.107(18)	0.39(8)
Sample (Trachybasalt)	Glass powder (mg)	$Ag_2C_2O_4$ (mg)	CO_2 (mg)	CO_2 (%)	CO_2 (CSA)	CO_2 (MIR)	CO_3^{2-} (MIR)	H_2O (MIR, %)
DTS1	812	5.80	1.68	0.21	0.27(7)	–	0.142(25)	0.48(6)
DTS3	807	6.13	1.78	0.22	0.24(3)	–	0.182(36)	0.39(13)

Notes: Calculated errors—last two digits—are shown in parentheses near values. Errors of the calculated contents of H_2O and CO_2, determined by Mid-Infrared (MIR) analyses, calculated by error propagation considering error of thickness (0.0002 cm), density (2 per cent relative), reproducibility of absorbance (for each band, respectively), and errors of the absorption coefficients. The bulk carbon content in the CO_2-bearing starting glasses was analysed using a Carbon-Sulfur Analyzer (CSA).

the 2-D analysed SEM section. However, following Bruce Watson & Brenan (1987, and reference therein), a sharp peak in the frequency distribution of measured apparent angles approaches the definition of the true angle, ϑ, values. Specifically, following the theoretical approach by Jurewicz & Jurewicz (1986), we estimated the median ϑ values to be within $\pm 3°$ from the mean value (Table 2). The range of median values should not be interpreted as the uncertainty in measured ϑ values, as it is not related to error estimation. Instead, a variability of true wetting angles also characterises systems with a complete textural equilibrium, for example as a consequence of anisotropies of interfacial energies in the system (Bruce Watson & Brenan 1987). In our analysis, we assume the median value of the apparent wetting angle, and associated standard deviation of the mean (SDM), to be the parameter of interest for the melt–crystal–CO_2 interfaces at equilibrium.

RESULTS

The CO_2-bearing glasses in the starting samples have bulk CO_2 contents ranging from ~2000 ppm for the trachyte to ~2700 ppm for the trachybasalt (Table 3). Mid-Infrared (MIR) analyses (Table 3) show that CO_2 is dissolved in the glass both as molecular CO_2 and $(CO_3)^{2-}$ groups. In light of the solubility data by Fanara *et al.* (2015), the total amount of CO_2 in the crystal-free glasses ranges between 1100 and 1600 ppm for both compositions, thus ensuring that the starting materials used for the decompression experiments are CO_2-saturated glasses.

The sets of trachytic and trachybasaltic samples rapidly quenched without decompression show virtually bubble-free groundmass and crystal rims, thus indicating that added CO_2 was efficiently dissolved in the melt. It has to be emphasised that the trachyte was completely molten at the experimental conditions, showing less than 2 per cent of microcrystals. At the lowest temperature the trachybasalt underwent a pervasive crystallization up to 50 per cent by volume, so that the vesiculation during decompression occurred in a latitic residual melt.

Being aware that an optimized experimental protocol for the study of bubble nucleation and growth has still to be developed, we rely on CO_2-saturated melts to investigate the crystal surface wettability from CO_2 bubble-crystal contact angles. In fact, for given melt composition and *P-T* boundary conditions, wettability is essentially controlled by the surface tension, σ, of the gas–melt–crystal interfaces (eq. 1).

Different from the experiments of Iacono Marziano *et al.* (2007a), focusing on H_2O bubble formation, in our experiments CO_2 bubble nucleation did not occur at the melt–AuPd capsule interface. The textures of samples obtained from decompressed runs show *HeN*
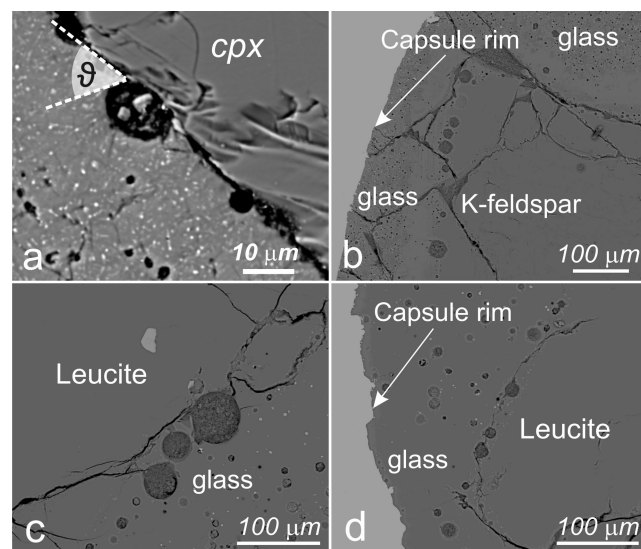

Figure 1. SEM images showing examples of heterogeneous nucleation (*HeN*) of CO_2 in a trachytic melt, from *HP-HT* decompression experiments ($T = 1125$ °C, decompression rate dP/d$t = 4.0$ MPa min^{-1}, initial pressure $P_0 = 312$ MPa, final pressure, $P_f = 30$ MPa). Details on experimental procedures are reported in Fanara *et al.* (2016).Vesicle-melt-crystal wetting relationships are expressed by the wetting angle, ϑ, defined as the angle between the crystal face and the tangent to the bubble face at the contact, measured through the melt (a). Clinopyroxene (a), K-feldspar (b), and leucite (c and d) crystals, which act as preferential sites for CO_2 bubble nucleation, with ϑ values of ~45°–55°, may lower the degree of supersaturation required for CO_2 bubble nucleation by 10–30 per cent (see eq. 2 in the text).

on different crystal surfaces, besides diffuse *HoN* in the groundmass (Fig. 1). Most of the experimental products from decompressed runs show a nearly unimodal bubble size distribution in the groundmass with bubble diameters ranging from 3 to 35 μm. Relatively larger vesicles with diameter up to 200 μm developed along K-feldspar and leucite crystal surfaces. The observed sizes of bubbles are much larger than the critical size of nuclei; for instance, the critical size of a H_2O bubble nucleus was estimated of ≤ 1 μm (Navon & Lyakhovsky 1998, and reference therein). Instead, bubble sizes in our experiments likely reflect some growth of the bubbles after nucleation.

Concerning the stability of mineral phases, by comparing non-decompressed and decompressed experiments, only K-feldspar in trachybasalt was not stable at the experimental conditions and recrystallized to plagioclase; for this reason, we do not report CO_2 wetting angles on K-feldspar in trachybasalt in our data set,
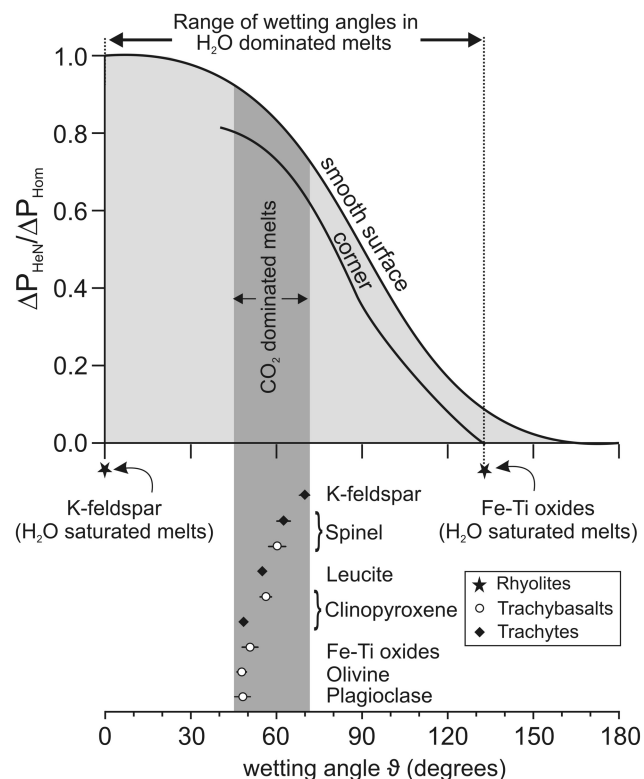
Figure 2. Supersaturation required for bubble nucleation, adimensionally expressed as the ratio between supersaturation in presence of crystals in the melt (ΔP_{HeN}) and supersaturation in crystal-free melt (ΔP_{Hom}), as a function of the wetting angle, ϑ (modified after Sigbee 1969). When $\vartheta = 0$, ΔP is that needed for the onset of homogenous nucleation. For other values of ϑ, and fixed ΔP and σ, $\Delta P_{\text{HeN}}/\Delta P_{\text{HoN}}$ is proportional to $\phi^{0.5}$ (see eq. 2 in the text). The two solid lines represent supersaturation conditions for *HeN* on crystals (i.e. smooth surfaces and edges, respectively). Wetting angles in CO_2-saturated, trachytic (solid diamonds) and trachybasalt (empty circles), melts for different mineral phases are reported. Horizontal bars are the standard deviation of the mean, SDM. For comparison, ϑ values for K-feldspar and Fe-Ti oxides in H_2O-saturated rhyolitic melts (black stars; data from Hurwitz & Navon 1994 and Gualda & Anderson 2007) are also reported.

while ϑ values reported in Table 2 refer to the trachyte case only. However, the crystallization of mineral phases such as K-feldspar and leucite may produce large volatile supersaturation pressures in cooling magmas without necessarily initiating bubble nucleation (Hurwitz & Navon 1994).

Values *of* ϕ obtained through wetting angles, ϑ (eq. 2), measured on the bubbles with diameter up to 35 μm illustrate the relative role of the different phenocrysts on the supersaturation conditions required for *HeN* of CO_2 (Table 2). Overall, it appears that, different from H_2O-dominated silicate melts, where mineral chemistry strongly controls the efficiency of crystals as sites for bubble nucleation (e.g. Hurwitz & Navon 1994), *HeN* in CO_2-saturated melts is poorly influenced by crystal composition (Fig. 2). In fact, ϑ values reported for H_2O-dominated systems (Hurwitz & Navon 1994; Gualda & Anderson 2007) vary over a wide range between $0°$ (feldspar and quartz crystals) and $\sim 135°$ (Fe-Ti oxides), whereas in CO_2-dominated melts we obtained ϑ mean values ranging between $\sim 47°$ for clinopyroxene to $\sim 70°$ for K-feldspar crystals, which correspond to a decrease in the ΔP required for CO_2 bubble nucleation of 20–37 per cent (Fig. 1; eq. 2).
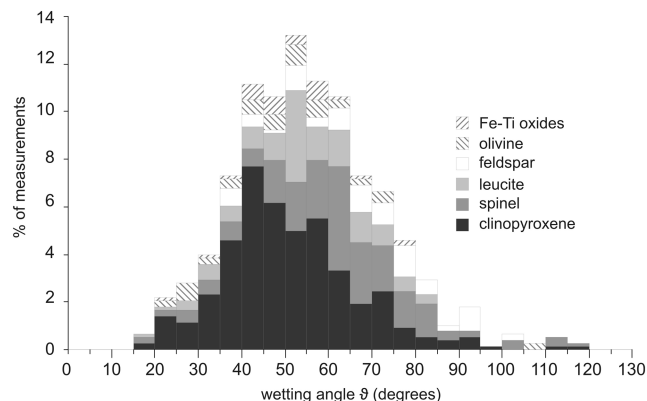

Figure 3. Cumulative distribution of CO_2 bubble wetting angles for different mineral phases in potassic melts. Total wetting angles determinations, $n = 760$, with a mean wetting angle value $\vartheta = 56° \pm 1°$ ($\pm$ SDM). Experimental conditions for trachyte and trachybasalt melt compositions and details on ϑ measurements for individual mineral phases are summarised in Table 2.

Fig. 3 reports a hystogram of the cumulative distribution of measured wetting angles ($n = 760$) for all crystal phases in trachyte and trachybasalt melts. It appears an overall unimodal pattern (modal $\vartheta = 56° \pm 1°$ SDM), possibly indicating a general effect of the surface energy anisotropy in CO_2-rich melts.

CONCLUDING REMARKS: IMPLICATIONS FOR ERUPTIVE DYNAMICS

Vesiculation (i.e. bubble nucleation and growth) as a consequence of magma decompression and/or volatile pressure build-up due to crystallization of anhydrous phases is a pre-requisite for explosive eruptions driven by magmatic volatiles. In addition, in a magma feeder system, the depth interval between early exsolution (where bubbles first appear) and the fragmentation levels can be large enough to allow the escape of volatiles, thus representing an attenuation mechanism for the explosivity of eruptions. Moreover, the effects of multicomponent gas exsolution (i.e. $H_2O + CO_2$), by inducing CO_2 depletion and H_2O enrichment as the magma approaches the surface (Mourtada-Bonnefoi & Laporte 2002), can result into significant variations of the efficiency of mineral phases as sites for bubble nucleation. Thus, volatile supersaturation and exsolution dynamics are much more complex than reproduced in the laboratory. Despite experimental simplifications, the results of the present study provide insights into the physics of bubble nucleation and growth into CO_2-bearing silicate melts. Overall, our findings point out that the *HeN* in CO_2-bearing silicate melts, independent of the crystallizing phases, lowers the supersaturation required for CO_2 bubble nucleation. As a consequence, magma vesiculation due to CO_2 exsolution can lead to earlier density decrease of H_2O-undersaturated magmas and to increased ascent rates relative to CO_2-free systems. Notably, anomalous and rapid CO_2 release at open vent mafic volcanoes (e.g. at Stromboli) is monitored as an indicator for imminent powerful explosive activity (Aiuppa *et al.* 2010).

This study provides a new data set (760 measurements) on CO_2-crystal wettability in potassic magmas, which sheds new light on the CO_2 behaviour in silicate melts. Here we address the effects of CO_2 heterogeneous nucleation on the dynamics of volatile exsolution in CO_2-rich magma systems with implications for volcanic hazard assessment. We propose that *HeN* in CO_2-rich magmas, along with

the peculiar mineral assemblage of potassic series, may represent a possible explanation for the shifting of high-K magma systems towards an apparently anomalous explosive behaviour. The new wetting angle data indicate that Fe-Ti oxide crystals ($\vartheta = 51 \pm 2°$ SDM) are moderately efficient sites for CO_2 bubble nucleation, although to a much lesser extent than in H_2O-dominated systems ($\vartheta \sim 160°$; Hurwitz & Navon 1994). Notably, K-feldspar ($\vartheta = 70 \pm 2°$ SDM) plays a significant role on CO_2 *HeN* in CO_2-dominated melts, leading to a decrease of ΔP up to 37 per cent (eq. 2), whereas in H_2O-dominated melts feldspar has no effect (Hurwitz & Navon 1994). Thus, K-feldspar, an almost ubiquitary mineral phase in explosive volcanism worldwide, may play an important role in determining the ascent rate and explosive behaviour of CO_2-bearing magma systems, as preferential site of CO_2 *HeN*. We remark that K-feldspar is a major phase controlling the differentiation of potassic magmas towards trachy-phonolitic terms. In particular, HP-HT experimental data evidence a very high rate of crystallization, for narrow temperature decrease, in trachytic melts (Trigila *et al.* 2008).

Also, ϑ data on leucite crystals ($55 \pm 1°$ SDM) evidence a significant effect on CO_2 *HeN* (decrease of ΔP up to 24 per cent) for this mineral phase typical of CO_2-rich, high-K magma systems, either co-existing with K-feldspar (e.g. in most of the Roman Province volcanoes, Palladino *et al.* 2014 and reference therein; also including Somma-Vesuvius), or as the dominant sialic phase (e.g. Colli Albani; Freda *et al.* 2011). In fact, phase diagrams for hydrous-carbonated phonotephritic melts show that the leucite stability field widens (relative to clinopyroxene) with decreasing pressure and increasing CO_2 concentration (Thompson 1977; Freda *et al.* 1997, 2008; Iacono Marziano *et al.* 2007b; e.g. see fig. 6c in Freda *et al.* 2011). In addition, experimental evidence from the phonolitic products of the 79 AD eruption of Somma-Vesuvius, shows that leucite attains 11.5–16.7 vol.% (corrected for vesicularity) at 100 MPa, while it reaches up to 21–31 vol.% at 50–25 MPa (Shea *et al.* 2009).

The syn-eruptive, rapid and pervasive leucite crystallization in K-rich magmas and, primarily in very low SiO_2, CO_2-dominated ultrapotassic magmas (e.g. Colli Albani, where leucite is virtually the only sialic phase; Freda *et al.* 1997, 2011), provides efficient sites for CO_2 *HeN*, which could potentially trigger a positive feedback mechanism among pressure decrease during magma ascent, extensive leucite crystallization, CO_2 saturation pressure drop and volatile exsolution at shallow depth, in turn leading to highly explosive behaviour. Finally, a better understanding of the dynamics of CO_2 degassing from magmas will improve our capability to interpret geochemical anomalies recorded at active volcanoes as possible precursors, such as the occurrence of intense episodes of CO_2 degassing before strong explosive events at mafic volcanoes.

REFERENCES

Aiuppa, A., Burton, M., Caltabiano, T., Giudice, G., Guerrieri, S., Liuzzo, M., Murè, F. & Salerno, G., 2010. Unusually large magmatic CO_2 gas emissions prior to a basaltic paroxysm, *Geophys. Res. Lett.,* **37,** L17303, doi:10.1029/2010GL043837.

Bower, S.M. & Woods, A.W., 1997. The control of magma volatile content and chamber depth on the mass erupted during explosive volcanic eruptions, *J. geophys. Res.,* **102,** 10 273–10 290.

Bruce Watson, E. & Brenan, J.M., 1987. Fluids in the lithosphere, 1. Experimentally-determined wetting characteristics of CO_2-H_2O fluids and their implications for fluid transport, host-rock physical properties, and fluid inclusion formation, *Earth planet. Sci. Lett.,* **85**(4), 497–515.

Deegan, F.M., Troll, V.R., Freda, C., Misiti, V., Chadwick, J.P., McLeod, C.L. & Davidson, J.P., 2010. Magma–carbonate interaction processes and associated CO_2 release at Merapi volcano, Indonesia: insights from experimental petrology, *J. Petrol.,* **51,** 1027–1051.

Ducker, W.A., 2009. Contact angle and stability of interfacial nanobubbles, *Langmuir,* **25**(16), 8907–8910.

Dunning, W.J., 1969. General and theoretical introduction, in *Nucleation*, pp. 1–67, ed. Zettlemoyer, A.C., Dekker.

Fanara, S., Botcharnikov, R.E., Palladino, D.M., Adams, F., Buddensieck, J., Mulch, A. & Behrens, H., 2015. Volatiles in magmas related to the Campanian Ignimbrite eruption: experiments vs. natural findings, *Am. Mineral.,* **100**(10), 2284–2297.

Fanara, S., Sottili, G., Silleni, A., Palladino, D.M. & Schmidt, B.C., 2016. CO_2 bubble nucleation and growth in potassium rich silicate magmas, *Chem. Geol,* doi:10.1016/j.chemgeo.2016.12.033.

Freda, C., Gaeta, M., Palladino, D.M. & Trigila, R., 1997. The Villa Senni Eruption (Alban Hills, central Italy): the role of H_2O and CO_2 on the magma chamber evolution and on the eruptive scenario, *J. Volc. Geotherm. Res.,* **78,** 103–120.

Freda, C., Gaeta, M., Misiti, V., Mollo, S., Dolfi, D. & Scarlato, P., 2008. Magma–carbonate interaction: an experimental study on ultrapotassic rocks from Alban Hills (Central Italy), *Lithos,* **101,** 397–415.

Freda, C., Gaeta, M., Giaccio, B., Marra, F., Palladino, D.M., Scarlato, P. & Sottili, G., 2011. CO_2-driven large mafic explosive eruptions: the Pozzolane Rosse case study from the Colli Albani Volcanic District (Italy), *Bull. Volcanol.,* **73,** 241–256.

Goff, F., Love, S.P., Warren, R.G., Counce, D., Obenholzner, J., Siebe, C. & Schmidt, S.C., 2001. Passive infrared remote sensing evidence for large, intermittent CO_2 emissions at Popcatépetl volcano, Mexico, *Chem. Geol.,* **177,** 133–156.

Gualda, G.A.R. & Anderson, A.T., 2007. Magnetite scavenging and the buoyancy of bubbles in magmas. Part 1: Discovery of a pre-eruptive bubble in Bishop rhyolite, *Contrib. Mineral. Petrol.,* **153**(6), 733–742.

Hirth, J.P., Pound, G.M. & St.Pierre, G.R., 1970. Bubble nucleation, *Metall. Trans.,* **1,** 939–945.

Holloway, J.R., 1976. Fluids in the evolution of granitic magmas: consequences of finite CO_2 solubility, *Bull. Geol. Soc. Am.,* **87,** 1513–1518.

Hurwitz, S. & Navon, O., 1994. Bubble nucleation in rhyolite melts: experiments at high pressure, temperature, and water content, *Earth planet. Sci. Lett.,* **122,** 267–280.

Iacono Marziano, G., Schmidt, B.C. & Dolfi, D., 2007a. Equilibrium and disequilibrium degassing of a phonolitic melt (Vesuvius AD79 "white pumice") simulated by decompression experiments, *J. Volc. Geotherm. Res.,* **161**(3), 151–164.

Iacono Marziano, G., Gaillard, F. & Pichavant, M., 2007b. Limestone assimilation and the origin of CO_2 emission at the Alban Hills (Central Italy): constraints from experimental petrology, *J. Volc. Geotherm. Res.,* **166,** 91–105.

Jaupart, C., 1998. Gas loss from magmas through conduit walls during eruption, in *The Physics of Explosive Volcanic Eruptions*, Vol. 145, pp. 73–90, eds Gilbert, J.S. & Sparks, R.S.J., Geol. Soc. Lond. Spec. Pub.

Jeffery, A. *et al.*, 2013. The pre-eruptive magma plumbing system of the 2007–2008 dome-forming eruption of Kelut volcano, Indonesia, *Contrib. Mineral. Petrol.,* **166,** 275–305.

Jolis, E.M., Troll, V.R., Harris, C., Freda, C., Gaeta, M., Orsi, G. & Siebe, C., 2015. Skarn xenolith record crustal CO_2 liberation during Pompeii and Pollena eruptions, Vesuvius volcanic system, central Italy, *Chem. Geol.,* **415,** 17–36.

Jurewicz, S.R. & Jurewicz, A.J.G., 1986. Distribution of apparent angles on random sections with emphasis on dihedral angle measurement, *J. geophys. Res.,* **91,** 9277–9282.

Landau, L.D. & Lifshitz, E.M. 1980. *Course of Theoretical Physics, Statistical Physics,* 3rd edn, Vol. 5, Pergamon.

Lasaga, A.C., 1998. *Kinetic Theory in the Earth Sciences*, Princeton Univ. Press.

Li, J., Chen, H., Zhou, W., Wu, B., Stoyanov, S.D. & Pelan, E.G., 2014. Growth of bubbles on a solid surface in response to a pressure reduction, *Langmuir,* **30**(15), 4223–4228.

Mourtada-Bonnefoi, C.C. & Laporte, D., 2002. Homogeneous bubble nucleation in rhyolitic magmas: an experimental study of the effect of H_2O and CO_2, *J. geophys. Res.,* **107**(B4), 2066, doi:10.1029/2001JB000290.

Navon, O. & Lyakhovsky, V., 1998. Vesiculation processes in silicic magmas, in *The Physics of Explosive Volcanic Eruptions,* Vol. 145, pp. 27–50, eds Gilbert, J.S. & Sparks, R.S.J., Geol. Soc. Lond. Spec. Pub.

Palladino, D.M., Gaeta, M., Giaccio, B. & Sottili, G., 2014. On the anatomy of magma chamber and caldera collapse: the example of trachyphonolitic explosive eruptions of the Roman Province (central Italy), *J. Volc. Geotherm. Res.,* **281,** 12–26.

Papale, P., 1999. Modeling of the solubility of a two-component $H_2O + CO_2$ fluid in silicate liquids, *Am. Mineral.,* **84,** 477–492.

Papale, P. & Polacci, M., 1999. Role of carbon dioxide in the dynamics of magma ascent in explosive eruptions, *Bull. Volcanol.,* **60,** 583–594.

Scandone, R., 1996. Factors controlling the temporal evolution of explosive eruptions, *J. Volc. Geotherm. Res.,* **72,** 71–83.

Schmidt, B.C., Holtz, F., Scaillet, B. & Pichavant, M., 1997. The role of H_2O-H_2 fluids and redox conditions on melting temperatures of quartzofeldspathic assemblages in the haplogranite system, *Contrib. Mineral. Petrol.,* **126,** 386–400.

Schuessler, J.A., Botcharnikov, R.E., Behrens, H., Misiti, V. & Freda, C., 2008. Oxidation state of iron in hydrous phono-tephritic melts, *Am. Mineral.,* **93,** 1493–1504.

Shea, T., Larsen, J.F., Gurioli, L., Hammer, J.E., Houghton, B.F. & Cioni, R., 2009. Leucite crystals: surviving witnesses of magmatic processes preceding the 79AD eruption at Vesuvius, Italy, *Earth planet. Sci. Lett.,* **281**(1–2), 88–98.

Sigbee, R.A., 1969. Vapor to condensed phase heterogeneous nucleation, in *Nucleation*, pp. 151–224, ed. Zettlemoyer, A.C., Dekker.

Sottili, G., Taddeucci, J. & Palladino, D.M., 2010. Constraints on magmawall rock thermal interaction during explosive eruptions from textural analysis of cored bombs, *J. Volc. Geotherm. Res.,* **192,** 27–34.

Thompson, R.N., 1977. Primary basalts and magma genesis. III Alban Hills, Roman Comagmatic Province, Central Italy, *Contrib. Mineral. Petrol.,* **60,** 91–108.

Trigila, R., Battaglia, M., Sottili, G. & Brilli, M., 2008. Volcanic eruptions from ghost magma chambers, *Geophys. Res. Lett.,* **35**(16), L16304, doi:10.1029/2008GL034579.

Wilson, L., Sparks, R.S.J. & Walker, G.P.L., 1980. Explosive volcanic eruptions—IV. The control of magma properties and conduit geometry on eruption column behaviour, *Geophys. J. R. astr. Soc.,* **63,** 117–148.

Yang, J., Duan, J., Fornasiero, D. & Ralston, J., 2007. Kinetics of CO_2 nanobubble formation at the solid/water interface, *Phys. Chem. Chem. Phys.,* **9**(48), 6327–6332.

Zhou, X.B. & De Hosson, J.Th. M., 1995. Influence of surface roughness on the wetting angle, *J. Mater. Res.,* **10**(8), 1984–1992.